JOURNAL OF GEOPHYSICAL RESEARCH, VOL. 106, NO. A12, PAGES 29,859-29,869, DECEMBER 1, 2001

Mapping Jupiter's outer radiation belt

R. S. Selesnick
The Aerospace Corporation, Los Angeles, California, USA

C. M. S. Cohen and E. C. Stone
California Institute of Technology, Pasadena, California, USA

Abstract. Flux maps of energetic ions in Jupiter's outer radiation belt, calculated with the aid of a model of the current sheet magnetic field, are consistent with a spatial distribution that is uniform along field lines and monotonically decreasing with radial distance. This result is supported by numerical ion trajectory calculations that predict uniform filling of drift shells at high L values. Adiabatic compression by radial transport then provides predictions of radial energy dependence and flux gradients. At lower L values, conservation of the second adiabatic invariant predicts some anisotropy with higher equatorial fluxes.

1. Introduction

Jupiter's outer radiation belt is contained in the magnetic field of the plasma sheet region, where the field lines are significantly distorted from those of the planetary dipole. This has complicated energetic particle data analysis so that results are typically reported only near the equatorial plane [*Kane et al.*, 1999; *Cohen et al.*, 2001]. Therefore little is known of particle spatial gradients in the direction perpendicular to the equatorial plane, which is critical to an understanding of the radiation belt dynamics. In this work we illustrate a solution of the problem by calculating maps of energetic ion fluxes for the outer radiation belt using a model of the current sheet magnetic field. We use data taken by the Galileo orbiter's Heavy Ion Counter (HIC), which measures ions with kinetic energies at and above several MeV/nucleon [*Garrard et al.*, 1992]. The motion of energetic ions in the plasma sheet region is known to be largely nonadiabatic [*Selesnick et al.*, 2001]. Therefore we also describe calculations of such motion and use the results to constrain a simulation of the ion spatial distribution for comparison with the observed flux maps.

2. Magnetic Field Model

Jupiter's planetary magnetic field at radial distances beyond 10 R_J is, to a good approximation, dipolar, but it is substantially modified by the field of the current sheet. We adopt the *Khurana* [1997] Euler potential model for the current sheet field (with the fourth set of parameters derived from Voyager and Pioneer data), combined with a centered dipole planetary magnetic field tilted by 9.6° from the rotation axis. No magnetopause or magnetotail current fields are included, although recent results have shown some local time dependences in the magnetic field [*Khurana*, 2001] and correspondingly in the energetic ions [*Cohen et al.*, 2001] caused by solar wind influence. These may be included in future magnetic field models but should have a negligible effect on our results.

The model magnetic field magnitude along the inbound Galileo G8 orbit in the region of interest is shown in Figure 1. Also shown for comparison is the unmodified dipole magnetic field. The strong modulation of the field due to the current sheet is a result of its offset from the orbital plane and the 10-hour rotation period of Jupiter. It illustrates the substantial diamagnetic reduction of the field in the current sheet and enhancement of the field outside it. Only a slight modulation is evident in the dipole field magnitude. The characteristic thickness of the model current sheet is 2 R_J, which represents an average derived from magnetic field data. However, the sheet thickness is variable and can change rapidly [*Selesnick et al.*, 2001]. To illustrate such variations, the sheet thickness parameter was changed from 2 R_J to values of 1 and 3 R_J, while maintaining a constant total sheet current, and the resulting field magnitudes are also shown in Figure 1. Variations in total sheet current are also possible but have a similar, though lesser, effect on the field magnitude because the field at the center of the current sheet is not modified. Therefore the examples of sheet thickness variations provide a reasonable error range for the model field and for the calculations to follow.

3. L Calculation

In a dipole magnetic field the L shell is the radial distance in planetary radii of a magnetic field line at its equatorial point. In a nondipolar field the generalized L is inversely proportional to the magnetic flux Φ through a particle drift shell [*Roederer*, 1970], so that Jupiter's current sheet reduces L to values less than the equatorial field line distances. If there were significant drift shell splitting due to azimuthal

Paper number 2001JA000061.
0148-0227/01/2001JA000061$09.00

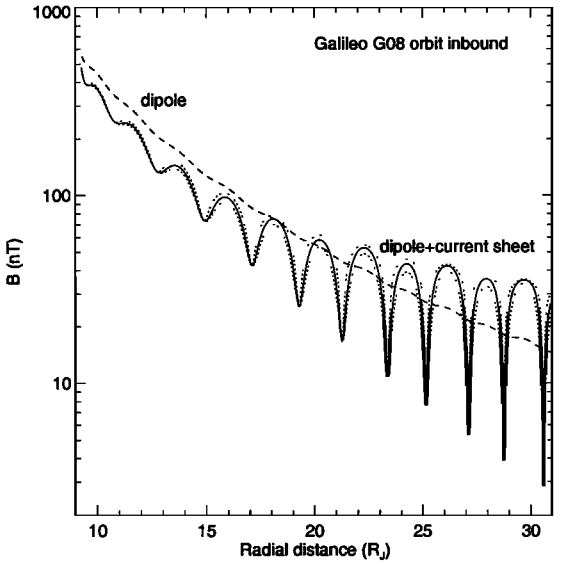

Figure 1. Model magnetic fields versus radial distance along the Galileo orbit. Dotted lines show an error range in the dipole plus current sheet model due to changes in current sheet thickness.

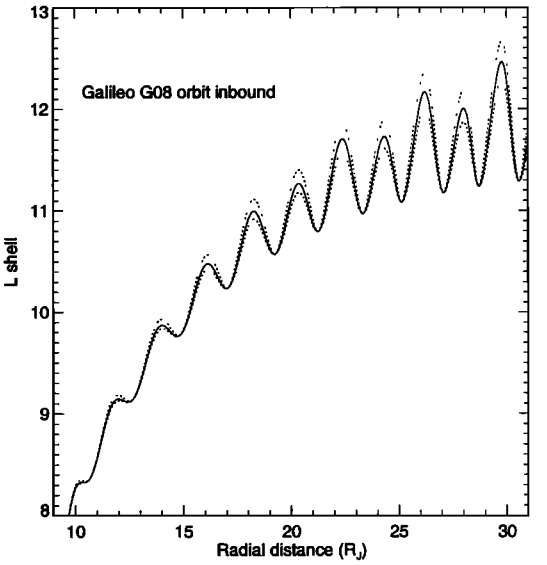

Figure 2. Model L values versus radial distance along the Galileo orbit. Dotted lines show an error range as before.

asymmetry in the magnetic field, then it would be necessary to calculate Φ. However, in our case, drift shell splitting is negligible because the dipole tilt introduces only a slight azimuthal asymmetry. The field of the current sheet becomes negligible relative to the dipolar planetary magnetic field near the dipole origin, so the L value can be accurately approximated as [*Schulz and Lanzerotti*, 1974]

$$L = \lim_{r \to 0} \frac{r}{R_J \sin^2 \theta}, \tag{1}$$

where r is radial distance and θ is the angle from the dipole axis and the limit is taken along the field line. This greatly simplifies the calculation because only a single numerical field line tracing is required to describe the magnetic flux enclosed by each drift shell and to uniquely label it with the L value.

The results of the L calculation (1) for the Galileo inbound G8 orbit are shown in Figure 2. The L values are substantially lower than the radial distance as discussed above. The modulation of the L values, caused by the current sheet moving above and below Galileo, is substantial because of the stretching of the magnetic field lines. Again the error range due to variations in current sheet thickness is shown. At the equatorial crossings, there is no uncertainty in L because the model equatorial magnetic field is independent of sheet thickness (as it is of total sheet current).

4. Pitch Angle Coverage

In particle motion conserving the first adiabatic invariant the distribution of particles along the field line is determined by the equatorial pitch angle distribution. These are not generally available from the HIC data, but some information on the field line distribution is available because the rocking of the plasma sheet caused by the dipole tilt means that the equatorial plane, defined by the minimum field magnitude values on each field line, oscillates relative to Galileo. The omnidirectional intensity measured at a location with field magnitude B on a field line with equatorial field magnitude B_0 includes particles with equatorial pitch angles in the ranges from zero to α_0 and $180°-\alpha_0$ to 180°, where, assuming adiabatic motion,

$$\sin^2 \alpha_0 = \frac{B_0}{B}. \tag{2}$$

The model values of α_0 for the inbound G8 orbit are shown In Figure 3. The measurements cover a substantial range

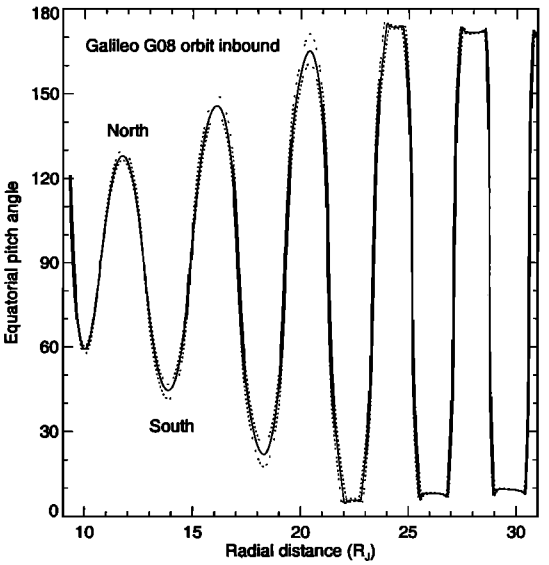

Figure 3. Equatorial pitch angle values for particles mirroring at the Galileo orbit versus radial distance, assuming conservation of the first adiabatic invariant. Values above (below) 90° indicate that Galileo was north (south) of the equatorial plane. Dotted lines show an error range as before.

of equatorial pitch angles because of the variation in B from relatively low equatorial values to relatively high values outside the plasma sheet. The range increases as the radial distance increases from 10 to 20 R_J, where it is nearly a full 180°. However, at the larger radial distances the time spent at intermediate pitch angles decreases and more of the time is spent observing only the equatorial pitch angles near zero and 180°. Similar conclusions apply to the other orbits. The large range of observable equatorial pitch angles is a result of the current sheet magnetic field and would not exist with only a dipole field (Figure 1).

Numerical calculations have shown that, in the HIC energy range, ion motion in the plasma sheet region at radial distances beyond ~20 R_J is largely nonadiabatic [*Selesnick et al.*, 2001], so that B and α_0 are not related by (2). The relevance of the nonadiabatic orbits and the utility of the the results described by Figure 3 under such circumstances are discussed in more detail following the data presentation.

5. Data

In this work we make use of data from two rate counters in the HIC LETB telescope [*Garrard et al.*, 1992; *Selesnick et al.*, 2001]. The rate called LB3 is from a single detector that responds primarily to protons in the kinetic energy range from 5 to 11 MeV. The rate that is itself called LETB is from a combination of detectors that responds only to heavy ions and, in the region of interest, primarily to oxygen ions in the kinetic energy range from 4 to 18 MeV/nucleon. The ion composition derived from the LETB data has been described by *Cohen et al.* [2001], and we are concerned primarily with the spatial distribution of this ion population. The fluxes measured by each rate counter are generally proportional to the omnidirectional intensity of the two ion populations. For the LETB rate we use 10 min averages of the data. For the LB3 rate, which has a lower time resolution that varies from ~10 to 50 min, we use all data points.

Data from six selected Galileo orbit segments in the radial range of 10 to 30 R_J are shown in Figure 4 as a function of radial distance from Jupiter. The time period covered is late 1996 to mid-1999 and each orbital segment lasted ~2 days. The data are modulated with a 5-hour period that reflects the rocking of the plasma sheet caused by Jupiter's rotation. The local rate maxima associated with the modulation occur at or near the minimum B equator, as shown by comparison with the field model calculations illustrated in Figure 1, and the values of the maxima generally decrease with radial distance. These observations contain significant information on the spatial distribution of the ions, but it cannot be interpreted directly from Figure 4 because the magnetic coordinates, L and B, are not included. The motion of Galileo in magnetic coordinates is complicated as shown by Figures 1 and 2.

The six orbit segments were chosen because they do not show strong evidence of temporal variations within each separate period and thereby provide good data sets for establishing the spatial distributions. Other Galileo orbits do show temporal variations in the HIC data which have been interpreted as evidence for ion acceleration in the ~25 to 30 R_J region [*Selesnick et al.*, 2001; *Cohen et al.*, 2001]. Some evidence of this type can be seen in Figure 4 with the data from the C21 orbit where the local maximum fluxes near 25 R_J stand out above the neighboring maxima. However, this is a minor exception, and the selected data generally show a smooth variation with radial distance.

6. Analysis Method

The B–L magnetic coordinate system is commonly used for radiation belt mapping [*McIlwain*, 1966; *Roederer*, 1970] because for a given particle drift shell described by a fixed L value, B describes the location relative to minimum B equator. Spatial variations across drift shells are therefore described by gradients in L and variations within a drift shell by gradients in B, eliminating the confusion of these two possibilities evident in the data format of Figure 4. The B and L coordinates for the inbound G8 orbit are illustrated in Figures 1 and 2, respectively, and similar results are obtained for the other orbits. Before presenting maps calculated from the data, we illustrate the method using synthetic data.

We first postulate a particle distribution that is proportional to L^{-30} with no B dependence and create synthetic LETB data from this distribution at 10-min intervals along the inbound G8 orbit in B–L coordinates. The results are shown in Plate 1 (left), where each data point is color coded by its flux value. We use the synthetic data to interpolate the flux to points on the map not covered by the orbit. This is done by triangulating the irregular grid in $\log B$ versus L formed by the data points, each pair of adjacent points forming the short side of a triangle with two long sides stretching a few tenths in L to a point on a nearby orbit segment. Each triangle forms a plane on which linear interpolation in the logarithm of the flux is then used to find flux contours over the entire shaded region shown in the figure. The contours are color coded in the same way as the data points. There is no unique way of interpolating the flux to the regions between the data points, but the contours show that at least in this case, our method reproduces the original distribution because the contours are independent of B and pass through the data points with the corresponding flux levels.

A second example is shown in Plate 1 (right). The same method was used, but the postulated distribution included a factor proportional to B_0/B or, equivalently in the case of adiabatic particle motion, to $\sin^2\alpha_0$. Again the contours accurately show the postulated B dependence of the spatial distribution. The extent to which the contours in this map depart from the straight, up and down contours of the previous example depends on the sizes of the postulated gradients in both B and L.

7. Flux Maps

Flux maps in B–L coordinates, based on the real data described in section 5, are shown in Plates 2 and 3 for the LETB and LB3 fluxes, respectively. The maps were calculated with same methods as those applied to the synthetic data in Plate 1.

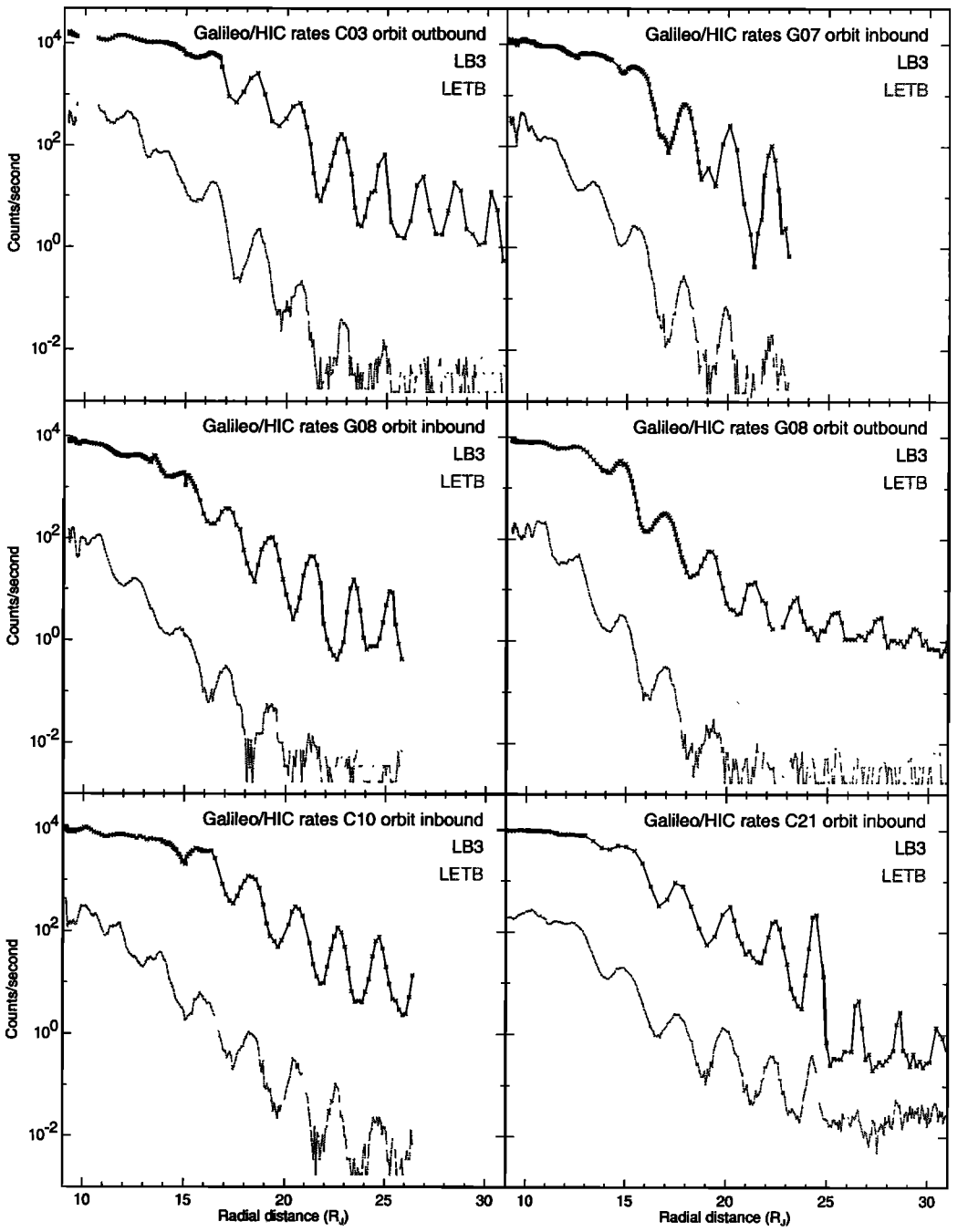

Figure 4. Particle fluxes from the Galileo/HIC LETB (bottom) and LB3 (top) rate counters versus radial distance for selected orbits.

Beginning with the LETB results in Plate 2, it is easy to see that the contours are generally consistent with a spatial flux distribution that is independent of B and decreases monotonically with L, as in the first synthetic map of Plate 1. This is particularly clear in the L range of ~9.5 to 10.5 where the LETB data generally have their greatest variability (Figures 2 and 4) and so are best suited to this type of analysis. It is also clear that the flux contours are not completely independent of B. The small B dependence does not show any systematic trend except in the region of $L \lesssim 9.5$, where there is some indication of decreasing flux with increasing B at a given L. We expect that the primary uncertainties in the flux map calculations are caused by errors in the model B and L coordinates (Figures 1 and 2) that can certainly cause some of the variability in the contour shapes, such as the discontinuities in their slopes that are sometimes seen as they cross the Galileo orbit. The method of interpolation may also introduce some uncertainty if the true spatial distributions are significantly different than those illustrated in the synthetic maps of Plate 1. Statistical errors in the counting rates are not significant, except at the lowest rates where contours are not shown.

Now considering the LB3 results in Plate 3, they again appear to be generally consistent with distribution that is independent of B and decreases monotonically with L. In this case, the result is most applicable in the L range from ~10 to

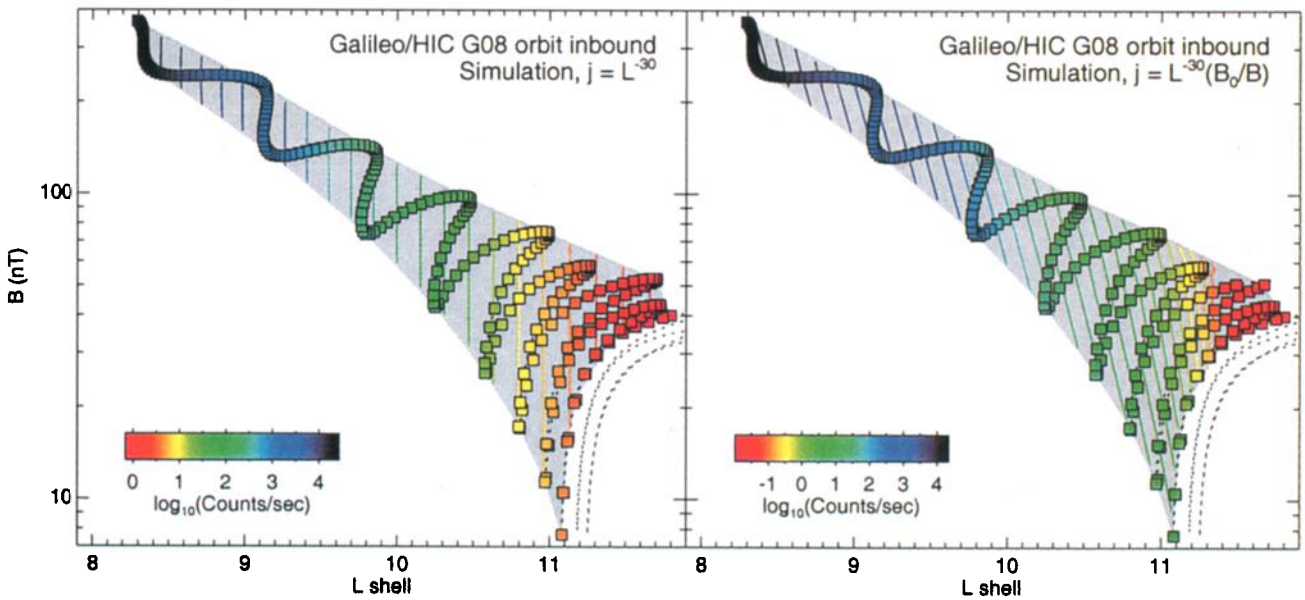

Plate 1. Synthetic flux maps for (left) isotropic and (right) anisotropic ion distributions. Note that differing color scales are used.

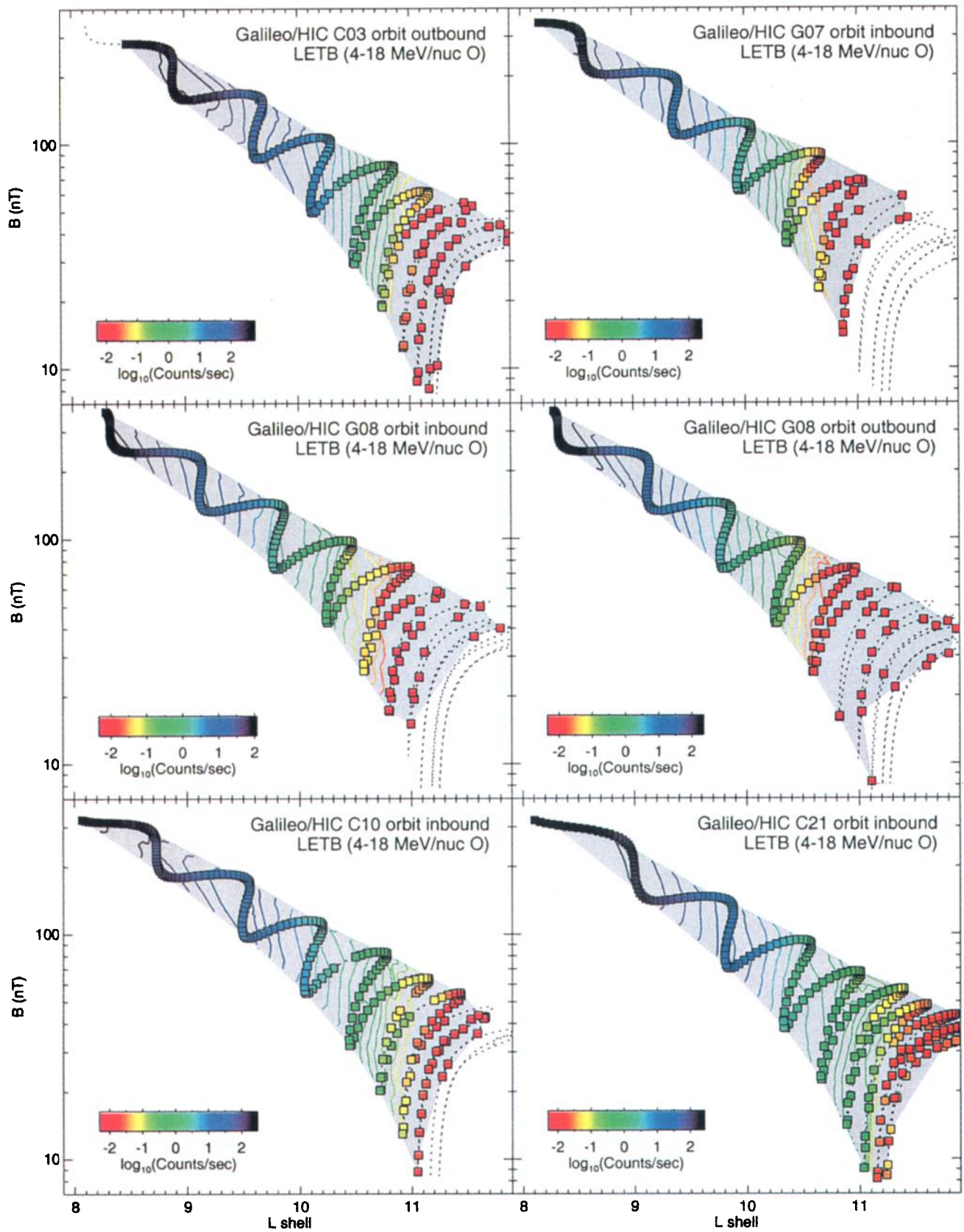

Plate 2. Flux maps from the LETB data for selected orbits in the radial range from 10 to 30 R_J. Contours calculated by interpolation of the color coded data points in the shaded region are shown at 0.2 decade intervals in flux. Data gaps are indicated by dotted lines. Note that differing color scales are used for each orbit.

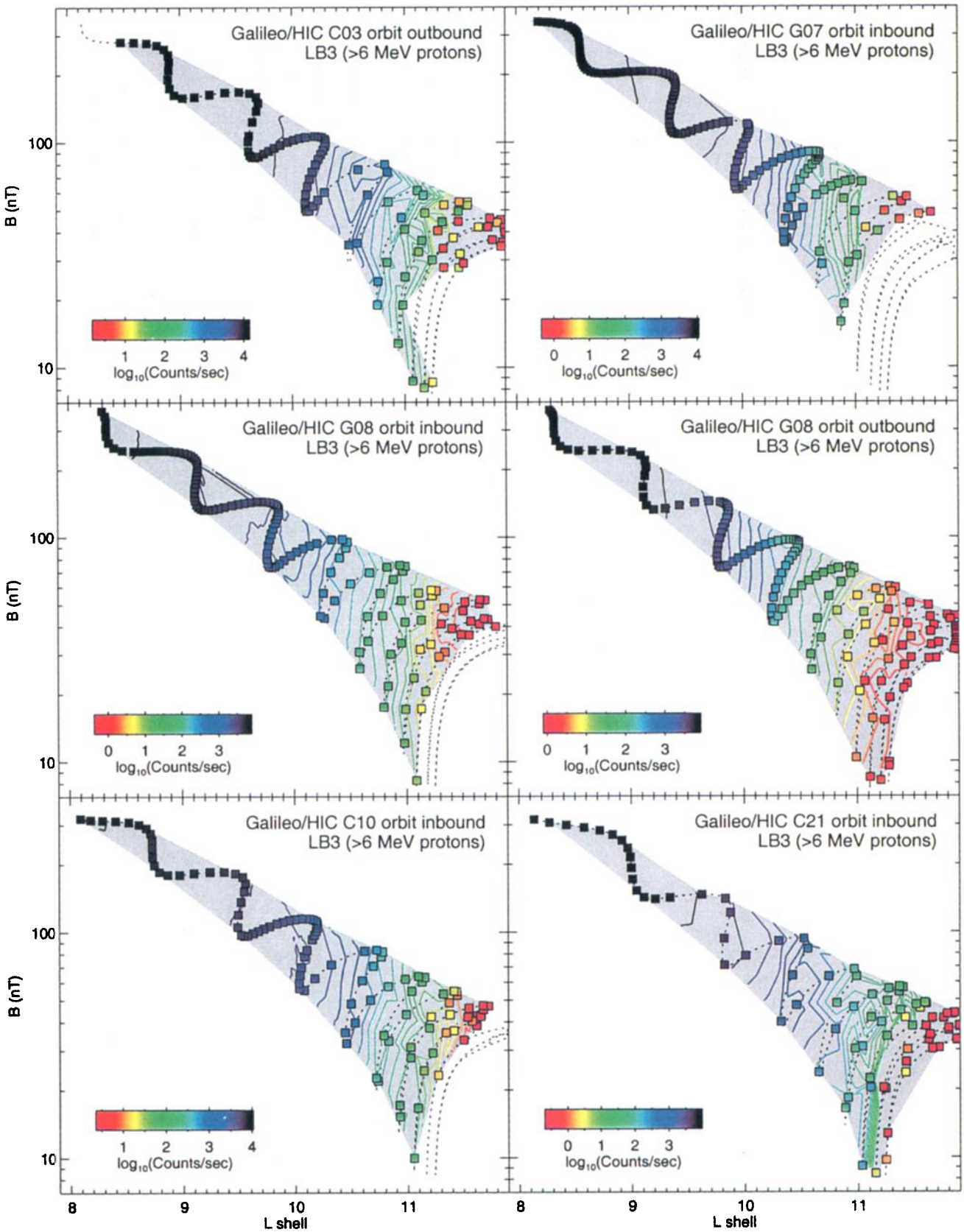

Plate 3. Flux maps from the LB3 data as in Plate 2.

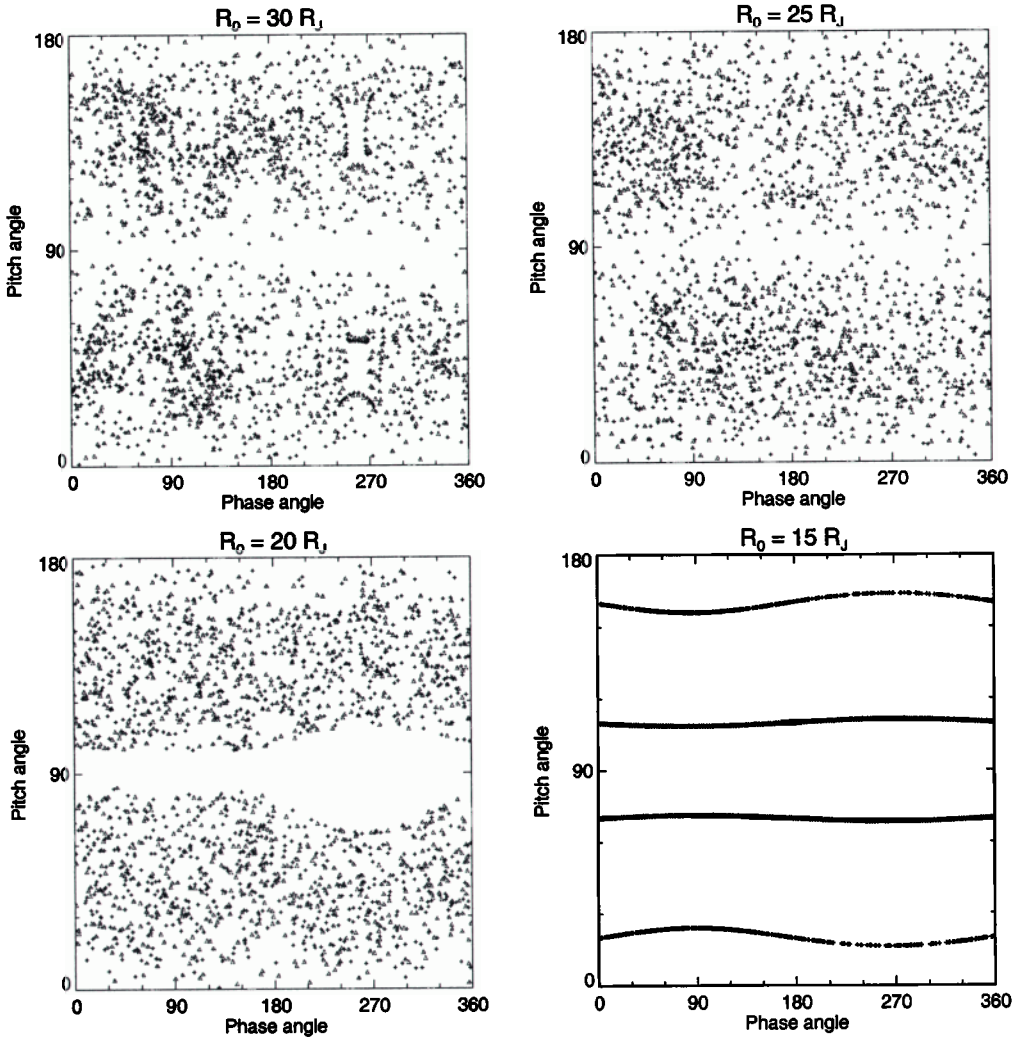

Figure 5. Simulated angular distributions for 173.5 MV ions at the equatorial plane and at varying initial radial distances R_0 calculated by numerical integration of ion trajectories.

11 because most of the variability in LB3 data, or relatively low energy ions, is at higher radial distances than the LETB data, or relatively high energy ions (Figure 4). In several locations, such as near $L = 10.5$ in the C3 orbit, the contours cannot be accurately determined because of the low LB3 time resolution. There are also greater uncertainties in the magnetic coordinates at the larger radial distances, and in the C21 orbit case at least, there is also some uncertainty caused by the temporal variations described previously. There is little variability in the LB3 rates at the lower L values, so that the contours in that region sometimes wander, as in the G8 orbit near $L = 9.5$.

8. Ion Trajectories

The results of section 7 should be interpreted in terms of ion trajectories. In the case where the trajectories conserve the first adiabatic invariant, the pitch angles and field magnitudes are related by (2) and the distribution of ions along a field line can be directly related to the pitch angle distribution. For example, a distribution that is independent of B at a given L is equivalent to an isotropic pitch angle distribution. In the case of nonadiabatic trajectories we can use numerical calculations of them to aid in the interpretation of the flux maps.

Previous numerical calculations [*Selesnick et al.*, 2001] characterized the properties of the nonadiabatic ion trajectories beyond ~20 R_J in Jupiter's current sheet. Here we use similar methods to study the transition between adiabatic and nonadiabatic trajectories. Some results are shown in Figure 5 for 173.5 MV rigidity, corresponding to 16 MeV protons or 4 MeV/nucleon O^{8+} ions, and in Figure 6 for 61.3 MV rigidity, corresponding to 2 MeV protons or 0.5 MeV/nucleon O^{8+} ions. Figures 5 and 6 show the magnetic pitch angles versus phase angles for each equatorial crossing of trajectories that were started at equatorial radial distances R_0 of 30, 25, 20, and 15 R_J (L =11.26, 11.06, 10.65, and, 9.80 respectively). At each radial distance, two trajectories were started, with initial pitch angles of 20° and 70°, and each was followed through 1000 equatorial crossings. The calculations use a simplified magnetic field model in which the dipole tilt is neglected, which does not effect the ion dynamics but makes the results easier to interpret (see *Selesnick et al.* [2001] for details).

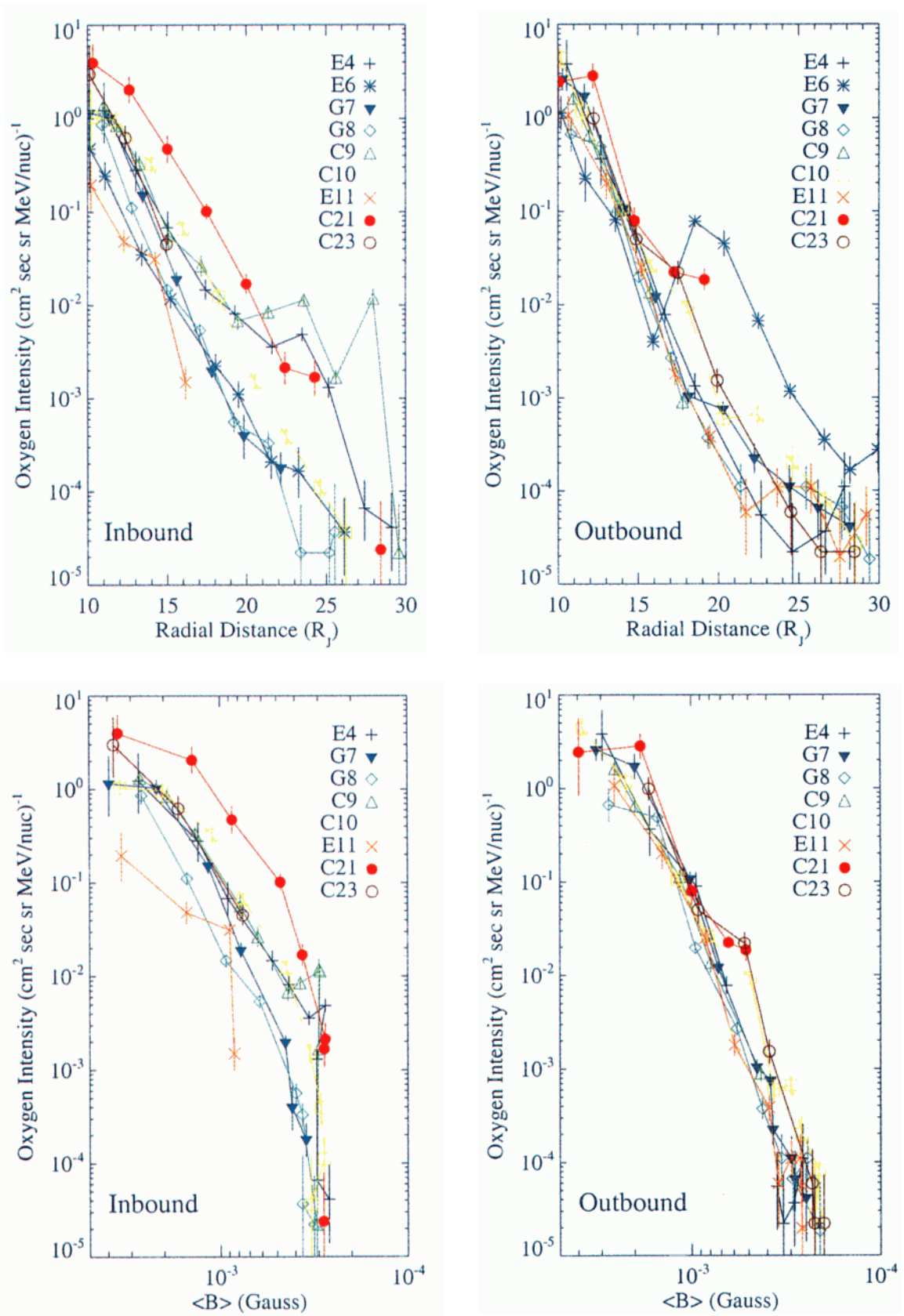

Plate 1. Oxygen intensities (~4-18 MeV nucleon^{-1}) for the inbound and outbound segments of each orbit (top) as a function of radial distance from Jupiter and (bottom) as a function of the average magnetic field magnitude. Note orbit E6 data are not presented in the bottom panels due to lack of magnetometer data for this orbit.

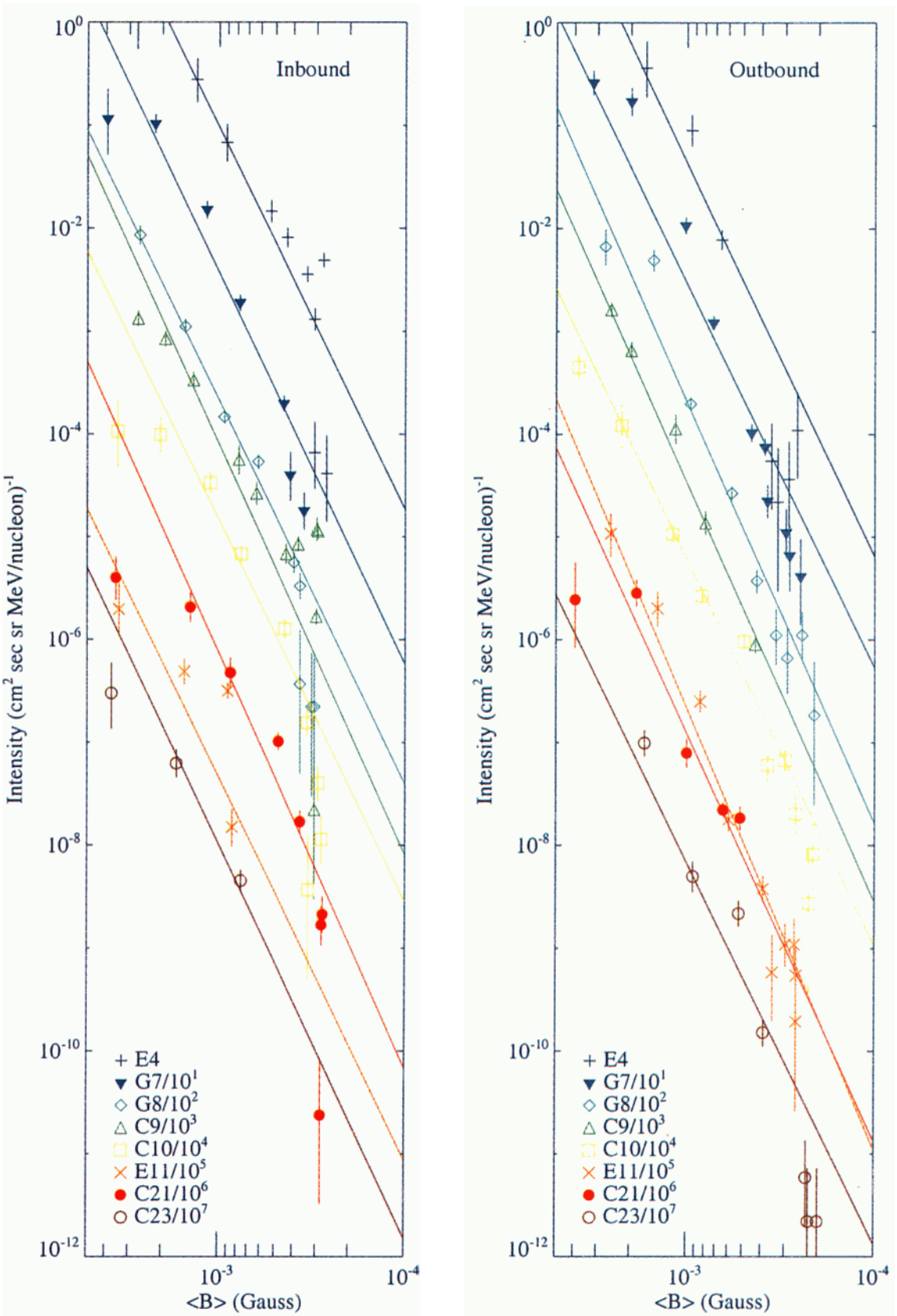

Plate 2. Oxygen intensities for the region 10-30 R_J for each orbit, inbound and outbound as a function of average magnetic field magnitude. The lines are the expected dependencies assuming lossless diffusion. Note that each orbit is shifted for clarity.

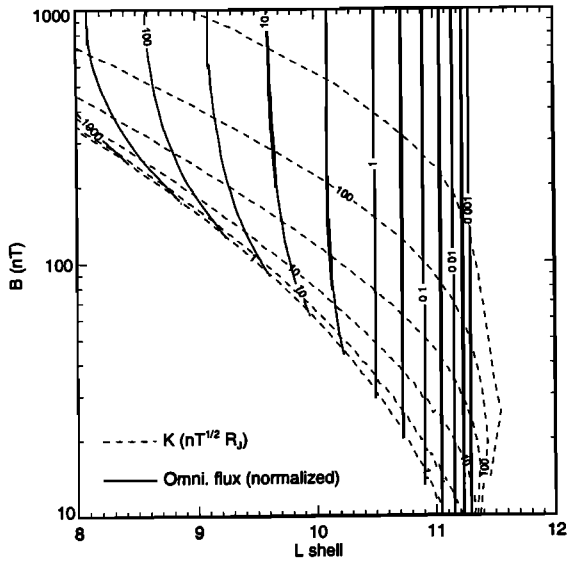

Figure 9. Simulated omnidirectional flux map for lossless inward radial diffusion, with contours every 0.5 decades, labeled each decade, and normalized at the $L = 10.5$ transition from nonadiabatic to adiabatic ion motion. Contours of the K invariant are also shown.

at $L = 9$ the omnidirectional intensity at the minimum B equator is ~4 times that at twice the equatorial B value. This is greater than any B dependence typically observed in the data. Most of the simulated B dependence is near the equator where it probably could not be resolved by the limited spatial coverage of the Galileo orbit, particularly at $L < 9.5$ where the data are less suited to providing accurate maps. However, it does appear that the simulation predicts more B dependence at the lower L values than is generally observed. This could be the result of an inaccurate location L_1 for the transition between adiabatic and nonadiabatic ion motion, or of additional pitch angle scattering at $L < L_1$. We have not accurately determined the L_1 value, because the data are not sufficient to constrain it, and it may well be time-dependent due to changes in the magnetic field configuration. Some variability between the flux maps from different orbits is evident.

11. Conclusions

The main result of this work is that flux maps of Jupiter's outer radiation belt derived from energetic ion data are approximately consistent with a spatial distribution that, in the $L \approx 9.5$ to 11 region (~14 to 25 R_J), is independent of magnetic field magnitude B at a given L shell while monotonically decreasing with L. This result is dependent on a realistic model of the current sheet magnetic field and on the accuracy of the derived magnetic coordinates. The data cover a substantial range of B values at a given L because of the rocking of the thin current sheet caused by Jupiter's rotation.

Results of numerical trajectory calculations support our interpretation of the energetic ion flux maps. They predict uniform filling of drift shells by nonadiabatic ion trajectories at radial distances beyond ~20 R_J ($L \approx 10.6$). In that region the energy of radially diffusing ions, and therefore the radial flux gradient, is controlled by the drift shell volume. As ions diffuse inward they reach adiabatic trajectories, but the isotropic pitch angle distribution obtained from the uniform flux at higher L shells should be maintained. As they continue to diffuse to lower L values the conservation of the second adiabatic invariant leads to some anisotropy with relatively higher equatorial fluxes, as shown by a simulated flux map. Some evidence for such distributions is seen in the data but with typically smaller anisotropies at the lower L values than predicted by the model.

Finally, the outer edge of Earth's electron radiation belt is also characterized by isotropic fluxes caused by nonadiabatic motion in the nightside plasma sheet [*Imhof et al.*, 1997]. In that case, electrons are quasi-trapped because their drift paths cross the magnetopause before reaching the dayside. Jupiter's ion radiation belt provides the first opportunity to study such isotropic fluxes in a stably trapped population.

Acknowledgments. This work was supported by NASA grant NAG5-8634 under the Jovian System Data Analysis Program.

Janet G. Luhmann thanks Christopher P. Paranicas and Thomas P. Armstrong for their assistance in evaluating this paper.

References

Birmingham, T. J., Pitch angle diffusion in the Jovian magnetodisc, *J. Geophys. Res.*, *89*, 2699–2707, 1984.

Cohen, C. M. S., E. C. Stone, and R. S. Selesnick, Energetic ion observations in the middle Jovian magnetosphere, *J. Geophys. Res.*, in press, 2001.

Garrard, T. L., N. Gehrels, and E. C. Stone, The Galileo heavy element monitor, *Space Sci. Rev.*, *60*, 305–315, 1992.

Imhof, W. L., D. L. Chenette, E. E. Gaines, and J. D. Winningham, Characteristics of electrons at the trapping boundary of the radiation belt, *J. Geophys. Res.*, *102*, 95–104, 1997.

Kane, M., D. J. Williams, B. H. Mauk, R. W. McEntire, and E. C. Roelof, Galileo energetic particles detector measurements of hot ions in the neutral sheet region of Jupiter's magnetodisk, *Geophys. Res. Lett.*, *26*, 5–8, 1999.

Khurana, K. K., Euler potential models of Jupiter's magnetic field, *J. Geophys. Res.*, *102*, 973–989, 1997.

Khurana, K. K., Influence of solar wind on Jupiters magnetosphere deduced from currents in the equatorial plane, *J. Geophys. Res.*, in press, 2001.

McIlwain, C. E., Magnetic coordinates, *Space Sci. Rev.*, *5*, 585–598, 1966.

Roederer, J. G., *Dynamics of Geomagnetically Trapped Radiation*, 166 pp., Springer-Verlag, New York, 1970.

Schulz, M., and L. J. Lanzerotti, *Particle Diffusion in the Radiation Belts*, 215 pp., Springer-Verlag, New York, 1974.

Selesnick, R. S., C. M. S. Cohen, and K. K. Khurana, Energetic ion dynamics in Jupiter's plasma sheet, *J. Geophys. Res.*, *106*, 18,895–18,906, 2001.

C. M. S. Cohen and E. C. Stone, California Institute of Technology, MC220-47, Pasadena, CA 91125, USA. (cohen@srl.caltech.edu)

R. S. Selesnick, The Aerospace Corporation, P.O. Box 92957-M2/259, Los Angeles, CA 90009-2957, USA. (richard.s.selesnick@aero.org)

(Received February 26, 2001; revised May 4, 2001; accepted June 7, 2001.)